Nuclear Science and Techniques (2026) 37:56
https://doi.org/10.1007/s41365-025-01875-1

Delocalization in the hot deformed hypernucleus $^{21}_{\Lambda}$Ne

Xin Li[1] · Chao-Feng Chen[2] · Qi-Bo Chen[1] · Xian-Rong Zhou[1]

Received: 24 April 2025 / Revised: 5 June 2025 / Accepted: 14 July 2025 / Published online: 23 January 2026

Abstract
We investigate the effects of temperature on the structural evolution and clustering in the hypernucleus, taking $^{21}_{\Lambda}$Ne as an example, in the framework of deformed finite-temperature Skyrme–Hartree–Fock. The SkI4 Skyrme force is employed for nucleon–nucleon interaction, while the NSC97f force is used for the hyperon–nucleon interaction. It is found that the system exhibits a strongly deformed ground state with pronounced α-cluster correlations and localized density distributions at low temperatures. As temperature increases, nuclear deformation weakens, the nuclear density spreads over the surface, and clustering gradually diminishes and vanishes entirely at $T \approx 2.8$ MeV. This is because that the thermal excitations lower the Fermi surface and enhance single-particle level splitting. In particular, owing to the lower excitation threshold of hyperons in the hypernuclear system, the hyperon radii exhibit a stronger temperature dependence than the nucleons. We further analyze the temperature-dependent changes in deformation, single-Λ binding energy, and entropy, providing new insights into the thermal evolution of the hypernuclear structure.

Keywords Finite temperature · Cluster structure · Hypernucleus · Skyrme–Hartree–Fock

1 Introduction

Hypernuclei are nuclear many-body systems that contain one or more bound hyperons within ordinary nuclei. Since the experimental discovery of the first hypernucleus in 1952 [1], different types of hyperons, such as Λ, $\Sigma^{+,0,-}$, and $\Xi^{0,-}$, have been identified. Unlike nucleons, a hyperon is not subject to the Pauli exclusion principle within the nucleus, allowing it to penetrate deeply into the center of a nuclear core. This unique property enables a hyperon to serve as a valuable probe for investigating nuclear properties that are otherwise inaccessible through conventional methods. The addition of a hyperon to the nucleus as an impurity has been shown to have significant effects on various aspects, including the modification of deformation [2–4], size [5, 6], and drip lines [7, 8]. Hypernuclei also provide an essential platform for testing hyperon–nucleon (YN) and hyperon–hyperon (YY) interactions, which are crucial for understanding the properties of multi-strange systems and their astrophysical applications [9–12].

Hyperons are believed to be abundantly present in the dense inner regions of neutron stars, where extreme temperature and density conditions prevail [13–15]. Experimentally, hyperons and hypernuclei are typically produced through high-energy beam collisions. Relativistic heavy ion collisions offer a distinctive methodology for generating hypernuclei and investigating nuclear matter under severe conditions characterized by elevated temperatures and densities. These processes facilitate the production of hypernuclei across a spectrum of sizes and isospin compositions, as the hyperons synthesized in these reactions are subsequently captured by either nucleons or nuclear fragments [16–18]. Recent experimental collaborations, including STAR [19, 20], ALICE [21, 22], and HypHI [23], have provided significant insights into hypernuclear production mechanisms, with additional measurements planned. Furthermore, experimental facilities such as PANDA [24], CBM [25], WASA@

This work was supported by the National Natural Science Foundation of China (Nos. 12575124, 12175071, and 12205103), and the National Key R&D Program of China (No. 2024YFE0109803), the Fundamental Research Funds for the Central Universities.

✉ Xian-Rong Zhou
xrzhou@phy.ecnu.edu.cn

[1] Department of Physics, East China Normal University, Shanghai 200241, China

[2] School of Physics Science and Engineering, Tongji University, Shanghai 200092, China

Super-FRS at FAIR [26], BM@N, MPD at NICA [27], and HFRS at HIAF [28] aim to further explore hypernuclear properties through relativistic particle-induced reactions [29]. Temperature plays a crucial role in the production of hypernuclei, as the short-lived nature of hypernuclei makes their formation highly temperature-dependent [30, 31]. Understanding the effects of temperature on hypernuclear properties is essential not only for interpreting experimental results but also for gaining insights into the behavior of hot nuclear matter, which has implications for astrophysical environments such as supernovae and neutron star mergers [32–35].

In recent years, several studies have investigated the properties of hypernuclei under finite-temperature conditions. For example, a study based on the relativistic Thomas–Fermi approach demonstrated that as the temperature increases, the radii of Λ hyperons expand more rapidly than those of nucleons, because it is easier to excite a small number of hyperons than to excite a large number of nucleons [36]. Furthermore, the finite-temperature Hartree–Fock–Bogoliubov (FT-HFB) framework has been applied to investigate the interplay between temperature and pairing correlations in multi-Λ hypernuclei, such as Ca, Sn, and Pb. The results reveal a critical temperature in agreement with the BCS prediction, as well as the emergence of a pairing re-entrance phenomenon in the ${}^{280}_{70\Lambda}$Pb hyperon drip-line hypernucleus [37].

The aforementioned studies have highlighted the impact of temperature on the hypernuclear structure, including modifications to the nuclear density distributions, which may influence nucleon localization and clustering behavior. For instance, clustering in nuclear matter is generally expected to occur under low-density and low-temperature conditions. Previous studies have focused primarily on the temperature effects on the clustering of nucleons in nuclear matter [38–42] and finite nuclei [43, 44]. Additionally, several investigations using both relativistic and non-relativistic nuclear energy density functionals have been conducted to understand the nuclear properties when the temperature increases [45–48]. While clustering in light nuclei at zero and finite temperatures has been extensively investigated, the effects of temperature on the localization and clustering in hypernuclei remain unknown. The presence of a hyperon introduces additional degrees of freedom and modifies nucleonic correlations, potentially affecting the formation and dissolution of clusters during thermal excitation. Gaining insight into these effects is important for a more comprehensive understanding of hypernuclear matter, particularly under thermal conditions relevant to astrophysical environments.

Over the past few decades, the Skyrme–Hartree–Fock (SHF) model has been widely and successfully applied to investigate normal nuclear structures (see, for example, Refs. [49–51]) and has also been extended to hypernuclear systems [52–59]. The clustering phenomenon in light stable and exotic nuclei has been explored within the SHF approach in Refs. [60–63].

This study aims to investigate the effects of temperature on the localization and clustering features of hypernuclei using the finite-temperature SHF model, offering new insights into their structure and interactions under extreme conditions. ^{20}Ne is a well-known nucleus characterized by a strong intrinsic quadrupole deformation and pronounced localization in its intrinsic densities [64–67]. To investigate the effect of temperature on clustering in hypernuclei, we selected ^{20}Ne as the core nucleus.

The remainder of this paper is organized as follows. In Sect. 2, the formalism of the finite-temperature SHF approach is introduced. The numerical details are presented in Sect. 3. In Sect. 4, we discuss the results of the binding energy, mean-field potentials, and density distributions in detail. Finally, a summary is given in Sect. 5.

2 Theoretical framework

Our calculations were performed using the self-consistent SHF model, which was extended to the theoretical description of hypernuclei in Refs. [54, 55, 68–70]. In this approach, the total energy of a hypernucleus can be written as [50]

$$E = \int \mathrm{d}^3\boldsymbol{r}\, \varepsilon(\boldsymbol{r}). \tag{1}$$

Here, ε is an energy density functional contributed by nucleons ε_{N} and hyperon ε_{Λ}

$$\varepsilon = \varepsilon_{\mathrm{N}}\left[\rho_{\mathrm{n}}, \rho_{\mathrm{p}}, \tau_{\mathrm{n}}, \tau_{\mathrm{p}}, \boldsymbol{J}_{\mathrm{n}}, \boldsymbol{J}_{\mathrm{p}}\right] + \varepsilon_{\Lambda}\left[\rho_{\mathrm{n}}, \rho_{\mathrm{p}}, \rho_{\Lambda}, \tau_{\Lambda}\right]. \tag{2}$$

They depend on the one-body density ρ_q, kinetic density τ_q, and spin–orbit current $\boldsymbol{J}_q$ as

$$\begin{aligned}
\rho_q &= \sum_{k\in\Omega_q} v_k^2 \left|\phi_q^k\right|^2, \\
\tau_q &= \sum_{k\in\Omega_q} v_k^2 \left|\nabla\phi_q^k\right|^2, \\
\boldsymbol{J}_q &= -\frac{i}{2}\sum_{k\in\Omega_q} v_k^2 \left[\phi_q^{k\dagger}\nabla\times\hat{\sigma}\phi_q^k - \phi_q^{k\dagger}(\nabla\times\hat{\sigma})^{\dagger}\phi_q^k\right].
\end{aligned} \tag{3}$$

$\phi_q^k\,(k = 1, ..., N_q)$ are the self-consistently calculated single-particle (s.p.) wave functions of the N_q occupied states for the different particles $q = \mathrm{n}, \mathrm{p}, \Lambda$ in a hypernucleus.

In the extension of the SHF model to the finite-temperature case, one merely replaces the occupation factor v_k^2 by a thermal Fermi distribution [71, 72]

$$\left(v_k^2\right)^{(\mathrm{therm})} = f_k = \frac{1}{1+\exp\left[\left(\varepsilon_k - \epsilon_{\mathrm{F},q_k}\right)/k_{\mathrm{B}}T\right]}, \tag{4}$$

at a given temperature T, where k_{B} is the Boltzmann constant.

The energy density functional ε_{N} represents the conventional nucleon–nucleon interaction [49]. The corresponding single-particle potential for neutrons or protons, V_{N}, can be expressed as:

$$V_{\mathrm{N}} = V_{\mathrm{N}}^{\mathrm{SHF}} + V_{\mathrm{N}}^{(\Lambda)}, \tag{5}$$

where $V_{\mathrm{N}}^{\mathrm{SHF}}$ arises from the Skyrme-type NN interaction [73], and $V_{\mathrm{N}}^{(\Lambda)}$ denotes the additional contribution from ΛN interaction. The ε_Λ is the hyperon–nucleon part and parameterized as (densities ρ given in units of fm^{-3}, energy density ε in $\mathrm{MeV}\cdot\mathrm{fm}^{-3}$) [74, 75]:

$$\begin{aligned}\varepsilon_\Lambda = &-\left(\varepsilon_1 - \varepsilon_2\rho_{\mathrm{N}} + \varepsilon_3\rho_{\mathrm{N}}^2\right)\rho_{\mathrm{N}}\rho_\Lambda \\ &+\left(\varepsilon_4 - \varepsilon_5\rho_{\mathrm{N}} + \varepsilon_6\rho_{\mathrm{N}}^2\right)\rho_{\mathrm{N}}\rho_\Lambda^{5/3},\end{aligned} \tag{6}$$

and together with Λ effective mass m_Λ^*

$$\frac{m_\Lambda^*}{m_\Lambda} \approx \mu_1 - \mu_2\rho_{\mathrm{N}} + \mu_3\rho_{\mathrm{N}}^2 - \mu_4\rho_{\mathrm{N}}^3, \tag{7}$$

the parameters ε_i in Eq. (6) and μ_i in Eq. (7) were obtained by performing Brueckner–Hartree–Fock calculations on hypernuclear bulk matter with the Nijmegen potential NSC97f [53].

Correspondingly, one obtains the SHF mean fields

$$\begin{aligned}V_{\mathrm{N}}^{(\Lambda)} =& \frac{\partial\varepsilon_\Lambda}{\partial\rho_{\mathrm{N}}} \\ &+ \frac{\partial}{\partial\rho_{\mathrm{N}}}\left(\frac{m_\Lambda}{m_\Lambda^*\left(\rho_{\mathrm{N}}\right)}\right)\left(\frac{\tau_\Lambda}{2m_\Lambda} - \frac{3}{5}\frac{\rho_\Lambda\left(3\pi^2\rho_\Lambda\right)^{2/3}}{2m_\Lambda}\right),\end{aligned} \tag{8}$$

$$V_\Lambda = \frac{\partial\varepsilon_\Lambda}{\partial\rho_\Lambda} - \left(\frac{m_\Lambda}{m_\Lambda^*\left(\rho_{\mathrm{N}}\right)} - 1\right)\frac{\left(3\pi^2\rho_\Lambda\right)^{2/3}}{2m_\Lambda}. \tag{9}$$

Through the variation of the total energy in Eq. (1), one derives the SHF Schrödinger equation for both nucleons and Λ hyperon,

$$\begin{aligned}&\left[-\boldsymbol{\nabla}\cdot\frac{1}{2m_q^*(\boldsymbol{r})}\boldsymbol{\nabla} + V_q(\boldsymbol{r}) - i\boldsymbol{W}_q(\boldsymbol{r})\cdot(\boldsymbol{\nabla}\times\boldsymbol{\sigma})\right]\phi_q^k(\boldsymbol{r}) \\ &= e_q^k\phi_q^k(\boldsymbol{r}).\end{aligned} \tag{10}$$

In the above formula, $\boldsymbol{W}_q(r)$ is the spin–orbit interaction part for nucleons, as given in Refs. [49, 50]. The $V_q(r)$ is the central part and is corrected by the effective mass term in Eq. (7).

By solving the Schrödinger equation, we can obtain the wave functions ϕ_q^k and single-particle energies e_q^k for the different single-particle levels k and species q. The standard nucleonic Skyrme force SkI4 [76] is applied in this study, but the results of the hyperonic observable are not sensitive to the choice of nucleonic force parameters [77].

Because the candidate core nuclei in this study are deformed, it is necessary to use the deformed SHF calculation. In the current work, axial symmetry is assumed for the SHF deformed potentials, and the Schrödinger equation is solved in cylindrical coordinates (r, z) [49, 50, 73]. The geometric quadrupole deformation parameter of the nuclear core is calculated as

$$\beta_2 \equiv \sqrt{\frac{\pi}{5}}\frac{\left\langle 2z^2 - r^2\right\rangle}{\left\langle r^2 + z^2\right\rangle}. \tag{11}$$

In the calculations, the quadrupole deformation β_2 spans the $[-0.2, 0.8]$ interval with steps of 0.02 to generate the potential energy surfaces.

In a nucleus or hypernucleus, the free energy is calculated by

$$F(\beta_2, T) = E(\beta_2, T) - TS(\beta_2, T), \tag{12}$$

where $E(\beta_2, T)$ is the total energy of the system for a given deformation parameter β_2 and temperature T. $S(\beta_2, T)$ is the entropy and defined as [45]

$$S = -k_{\mathrm{B}}\sum_k\left[f_k\ln f_k + \left(1-f_k\right)\ln\left(1-f_k\right)\right], \tag{13}$$

where f_k is given by Eq. (4).

The relevant finite-temperature properties can be calculated from the lowest state on the free energy surface, characterized by a quadrupole deformation β_2^* at a given temperature T. $P(\beta_2, T)$ is a mathematical expression for the probability that a system in equilibrium obtains a deformed configuration with a quadrupole parameter β_2 at finite temperature [78].

$$P\left(\beta_2, T\right) \propto \exp\left[-\Delta F\left(\beta_2, T\right)/T\right]. \tag{14}$$

Here, $\Delta F\left(\beta_2, T\right)$ is the free energy difference between a given deformation and temperature state and the lowest free energy state

$$\Delta F\left(\beta_2, T\right) = F\left(\beta_2, T\right) - F\left(\beta_2^*, T\right). \tag{15}$$

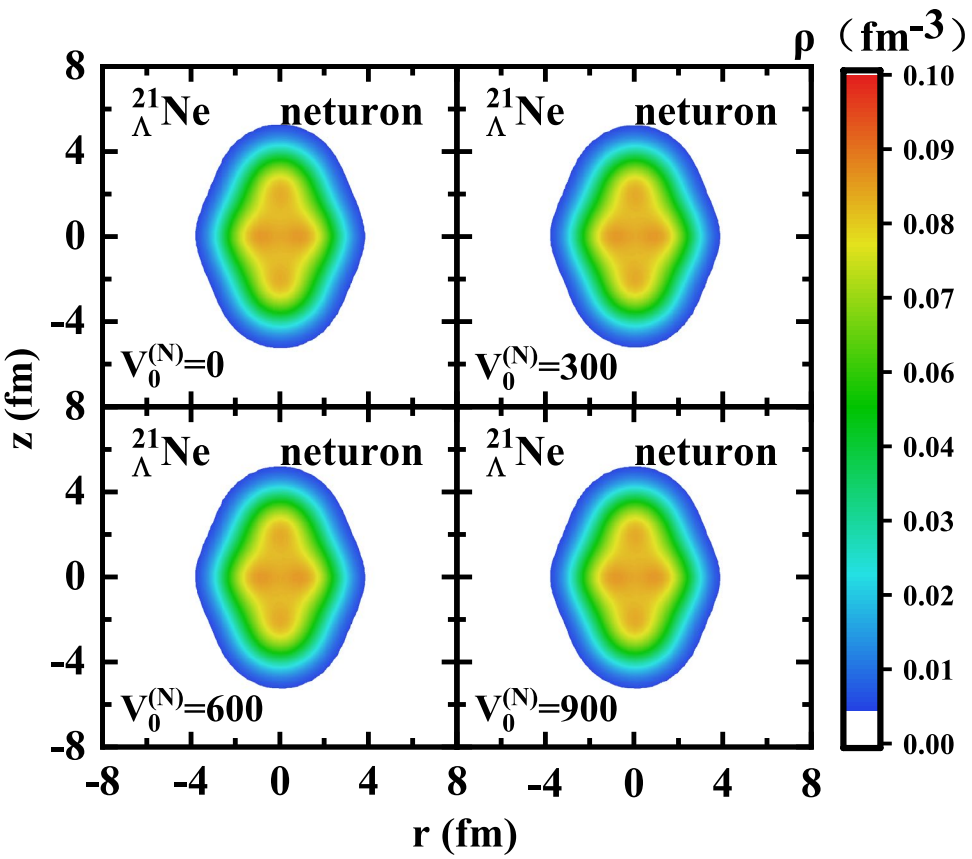

Fig. 1 (Color online) The neutron density distributions for $^{21}_{\Lambda}$Ne at zero temperature with varying pairing strengths. The four panels correspond to pairing strengths of 0, 300, 600, and 900 MeV · fm^3, respectively

In the theoretical modeling of nuclei and hypernuclei at finite temperatures, both statistical and quantum fluctuations must be considered. Quantum fluctuations are particularly significant for light nuclei and at low temperatures ($T < 1$ MeV), but play a minor role for nuclei with a sharp minimum in their free energy surface [79, 80]. In mesoscopic systems, such as finite nuclei and hypernuclei, statistical fluctuations around the minimum free energy are expected to make a notable contribution at finite temperatures. Therefore, in this study, we focused solely on statistical fluctuations in our calculations. To account for these effects, the thermal average of an observable $\bar{O}$ is obtained by mixing the expectation values $O(\beta_2, T)$ at various deformations β_2 using the ensemble average [43, 81]:

$$\bar{O} = \frac{\int \mathrm{d}\beta_2 O(\beta_2, T) \exp\left(-\Delta F(\beta_2, T)/T\right)}{\int \mathrm{d}\beta_2 \exp\left(-\Delta F(\beta_2, T)/T\right)}. \tag{16}$$

3 Numerical details

In this study, the properties of hot Λ hypernucleus $^{21}_{\Lambda}$Ne are investigated within the framework of the finite-temperature SHF model. For the nucleon–nucleon (NN) interaction, the Skyrme force SkI4 is employed, which provides an excellent overall fit to the ground-state properties of nuclei ranging from ^{16}O to ^{208}Pb, as well as the isotope shifts in Ca and Pb isotopes [76]. For the hyperon–nucleon YN interaction, microscopic Nijmegen interaction NSC97f [53] is employed, which is derived from Brueckner–Hartree–Fock (BHF) calculations of hypernuclear matter. It was successfully applied to calculate the ground-state properties of single- and multi-Λ hypernuclei [55, 63].

Pairing effects are often considered to play an important role in some nuclear phenomena. To quantify the effect of pairing correlations on the density distribution, we performed additional calculations for $^{21}_{\Lambda}$Ne at $T = 0$ MeV using a density-dependent δ pairing interaction in the BCS approximation. The interaction strength for nucleons was taken as $V_0^{(\mathrm{N})} = 0$, 300, 600, and 900 MeV · fm^3, respectively. Figure 1 demonstrates that the nuclear density distributions of $^{21}_{\Lambda}$Ne exhibit negligible variations ($\Delta\rho/\rho_{\max} < 0.2\%$) across all pairing strengths. Moreover, from a theoretical perspective, the omission of pairing correlations is supported by two considerations. First, the ground state of ^{20}Ne features a relatively large single-particle energy gap near the Fermi surface, which suppresses the pairing correlations at zero temperature. Second, at finite temperature, thermal excitations weaken pairing correlations, leading to the collapse of the pairing gap beyond a critical temperature of approximately $k_{\mathrm{T}} \sim 0.7$ MeV [82, 83]. These observations suggest

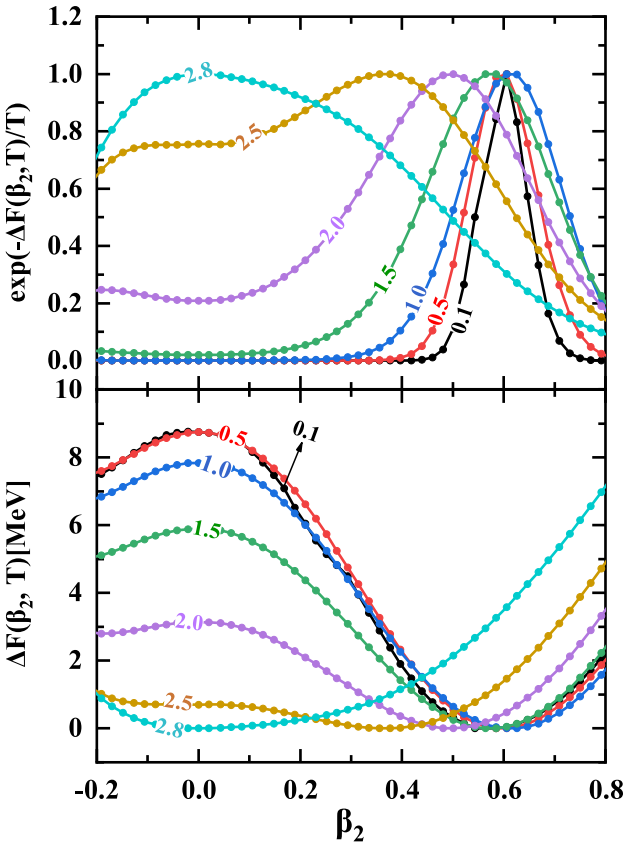

Fig. 2 (Color online) Relative free energies $\Delta F(\beta_2, T)$ (lower panel) and the corresponding probability factors $\exp\left[-\Delta F\left(\beta_2, T\right)/T\right]$ (upper panel) as functions of quadrupole deformation parameter β_2 at finite temperatures $T = 0.1$, 0.5, 1.0, 1.5, 2.0, 2.25, 2.5, and 2.8 MeV for $^{21}_{\Lambda}$Ne

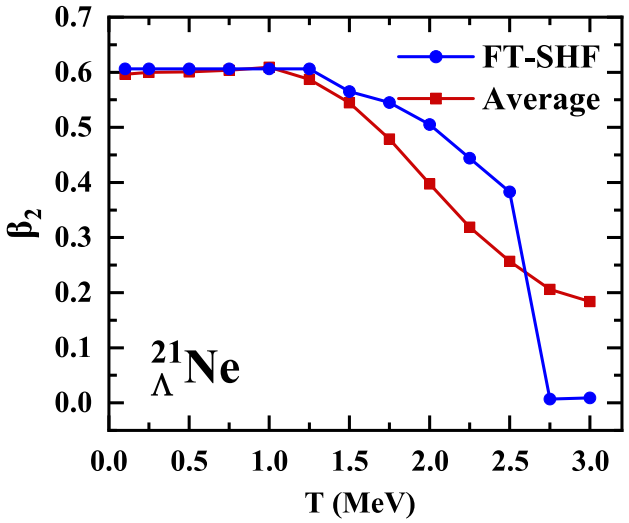

Fig. 3 (Color online) The evolution of the quadrupole deformation parameter β_2 with temperature. The most probable values (circles) correspond to the deformation at the free energy minimum, while the thermal average values (squares) are calculated using the constrained FT-SHF results at finite temperatures according to Eq. (16)

that the pairing effects are negligible within the temperature regime of interest. Therefore, it is justifiable to exclude pairing correlations in this study, as it simplifies the calculations while allowing us to focus on the temperature effects on the clustering behavior.

4 Results and discussion

Figure 2 presents the free energy surfaces and probability factors as functions of deformation at finite temperatures. The probability factor, as defined by Eq. (15), is determined by the free energy and temperature with $\exp[-\Delta F(\beta_2, T)/T]$.

At $T = 0.1$ MeV, the free energy surface exhibits a well-defined minimum around $\beta_2 = 0.60$, corresponding to a probability factor of 1. This indicates a stable configuration characterized by a robust quadrupole deformation and well-defined clustering.

As the temperature increases from 0.1 to 2.8 MeV, thermal excitations enhance the probability of populating a wider range of deformed states, reducing the dominance of the $\beta_2 \approx 0.6$ minimum. Concurrently, the free energy surface flattens, leading to an increase in the contribution of other states to the thermal average of observables, as evidenced by the changes in the probability factors. This behavior reflects the gradual weakening of the spatial localization and clustering in $^{21}_{\Lambda}$Ne.

As the temperature increases, the hypernuclear system gradually reduces its tendency for strong quadrupole deformation, which is observed at lower temperatures. The nuclear shape transitions to a more symmetric configuration, resulting in the dissolution of the clustering structures. This highlights the strong thermal sensitivity of clusters.

To analyze the effect of thermal shape fluctuations at a finite temperature, we evaluate the thermal average of the quadrupole deformation parameter using Eq. (16), as shown in Fig. 3. As expected, once thermal fluctuations are included, the sharp shape phase transition is smoothed out, and the decrease in β_2 becomes more gradual with increasing temperature. Although the average deformation remains small, it does not vanish even at $T = 3.0$ MeV, indicating that thermal fluctuations effectively wash out abrupt structural transitions.

We further studied the changes in the localization properties and behavior of the α clusters in $^{21}_{\Lambda}$Ne with increasing temperature. Figure 4 presents the density distributions of the Λ hyperon (left panels) and neutrons (middle panels) in $^{21}_{\Lambda}$Ne at different temperatures. Both hyperon and neutron density distributions show reduced

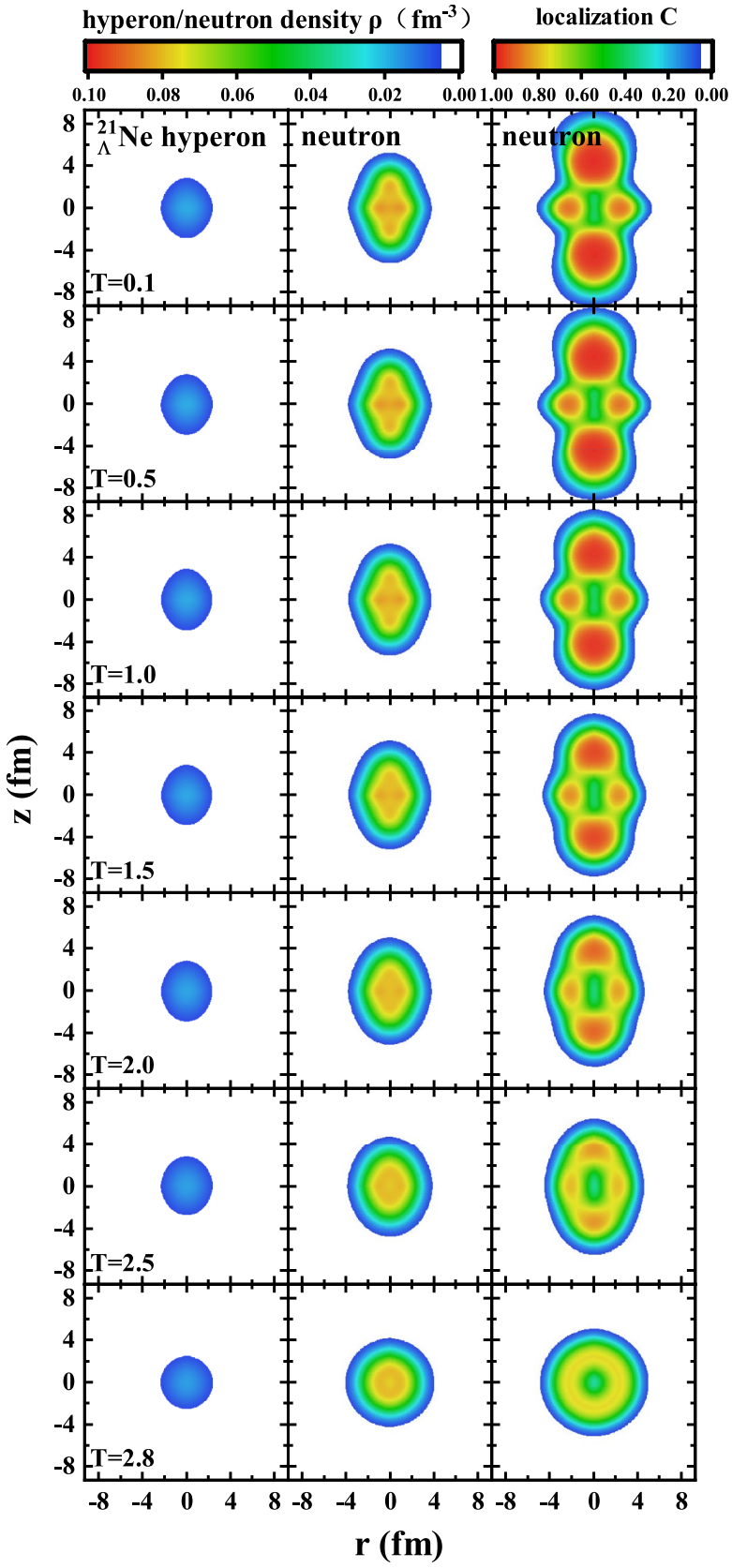

Fig. 4 (Color online) The density distributions of hyperon (left panels) and neutron (middle panels) as well as the neutron localization function (right panels) for ${}^{21}_{\Lambda}$Ne at finite temperatures $T = 0.1$, 0.5, 1.0, 1.5, 2.0, 2.5, and 2.8 MeV, respectively

deformation with increasing temperature, transitioning from prolate at $T = 0.1$ MeV to spherical at $T = 2.8$ MeV. The reduction in deformation primarily results from the depopulation of deformation-driven states and the vanishing of shell effects at elevated temperatures [84]. It should be emphasized that the results presented in Fig. 4 are obtained from the configurations corresponding to the free energy minima at each temperature. Consequently, thermal shape fluctuations were not explicitly incorporated into these plots. This approach allows for a clearer visualization of the intrinsic clustering features and the gradual reduction of deformation with increasing temperature. In contrast, performing thermal averaging over deformed configurations obscures fine structural details, complicating the analysis of temperature-induced modifications to the cluster structure, which is the primary focus of this section.

The deformation of both nuclei and hypernuclei is generally determined by the single-particle energy levels occupied by nucleons that are close to the Fermi surface. The energy density functional method provides an understanding of this phenomenon by utilizing nucleon density distributions. However, the nucleon density distribution is the result of the accumulation of all occupied single-particle energy levels; thus, it loses a signiticanty amount of detailed information.

In this study, we employed the localization function, which incorporates contributions from the kinetic energy, density, and current density, to provide a more comprehensive analysis of the nuclear localization structure [6, 85, 86]. It can be written as the probability of finding the second particle located within a shell of small radius around the assumed particle at r with the same spin σ ($\uparrow$ and $\downarrow$) and isospin q (= n, p, or Λ) [60], and is given by

$$\mathcal{C}_{q\sigma}(\boldsymbol{r}) = \left[1 + \left(\frac{\tau_{q\sigma}\rho_{q\sigma} - \frac{1}{4}\left[\nabla\rho_{q\sigma}\right]^2 - \boldsymbol{j}_{q\sigma}^2}{\rho_{q\sigma}\tau_{q\sigma}^{\mathrm{TF}}}\right)^2\right]^{-1}, \tag{17}$$
$$\tau_{q\sigma}^{\mathrm{TF}} = \frac{3}{5}\left(6\pi^2\right)^{2/3}\rho_{q\sigma}^{5/3},$$

where the kinetic energy density $\tau_{q\sigma}$, particle density $\rho_{q\sigma}$, and current density $j_{q\sigma}$ are given by Eq. (3). The localization function $\mathcal{C}_{q\sigma}(\boldsymbol{r})$ provides a dimensionless and normalized measure of nucleon localization. For light $N = Z$ even-even nuclei, the localization distributions of protons ($\mathcal{C}_{\mathrm{p}}$) and neutrons ($\mathcal{C}_{\mathrm{n}}$), as well as spin-up ($\mathcal{C}_{\uparrow}$) and spin-down ($\mathcal{C}_{\downarrow}$) states, exhibit considerable similarity owing to the small Coulomb interaction and fully occupied single-particle energy levels [60]. Consequently, a single parameter, ($\mathcal{C}_{\mathrm{n}\uparrow}$), adequately describes all previously mentioned parameters including ($\mathcal{C}_{\mathrm{p}\uparrow}$), ($\mathcal{C}_{\mathrm{p}\downarrow}$), ($\mathcal{C}_{\mathrm{n}\uparrow}$), and ($\mathcal{C}_{\mathrm{n}\downarrow}$).

Owing to the above convenience, the current study utilizes the localization distribution of spin-up neutrons ($\mathcal{C}_{\mathrm{n}\uparrow}$) as the nucleon localization distribution $\mathcal{C}$ to investigate the structure of localized clusters in ${}^{21}_{\Lambda}$Ne. The neutron localization function of ${}^{21}_{\Lambda}$Ne is displayed in the right panel of Fig. 4 at various temperatures. When the nucleon localization is close to 1, α-like clusters (a pure overlap of four nucleon wave functions) are expected because of spin and isospin degeneracy. Compared to the density profiles, the localization function typically displays a larger spatial extension because of the kinetic term included in the calculation.

At low temperatures, the localization function predicts highly localized regions at the outer ends, and the α clusters are clearly visible for ${}^{21}_{\Lambda}$Ne. The localization feature is also obtained around the center, which is associated with ^{12}C. Therefore, this pattern is interpreted as α-^{12}C-α quasimolecular configuration [87]. The cluster structures remain robust up to $T = 1.0$ MeV. Beyond this temperature, thermal excitations induce nucleon delocalization, resulting in the gradual suppression of clustering signatures. As the temperature increased further, enhanced thermal fluctuations led to the progressive dissolution of the cluster structures. Ultimately, the clustering effects vanish before the nucleus undergoes a shape phase transition at $T = 2.8$ MeV. These findings are in agreement with the results obtained from the total intrinsic density distributions shown in the middle panels of Fig. 4, providing further insights into the thermal evolution of nuclear clustering phenomena.

As the temperature increases, the clustering in hypernuclei gradually weakens and eventually disappears. This phenomenon is closely linked to the thermal evolution of single-particle energy levels. To investigate these thermal effects, Fig. 5 presents the Nilsson single-particle level diagram for neutrons.

First of all, Fig. 5 shows that as the temperature increases, the Fermi surface shifts downward. This shift occurs because thermal excitation promotes more nucleons to higher-energy states, and to conserve the total particle number, the Fermi level must decrease to compensate for the increased occupation of high-energy levels. The Fermi–Dirac distribution further modifies the occupation probabilities near the Fermi surface.

Second, in deformed nuclei, the $1d_{5/2}$ orbit is split into multiple energy states owing to the combined effects of the deformation potential and spin–orbit interaction. As the temperature increases, nucleons become increasingly excited to higher angular momentum orbitals, leading to an enhancement of the spin–orbit coupling. This, in turn, amplifies the energy separation between split states. The effect is particularly evident in the pronounced energy gap between the [202 5/2] and [211 1/2] orbitals at small deformations.

To further investigate the temperature-dependent behavior of the hyperon, we analyzed its Nilsson single-particle

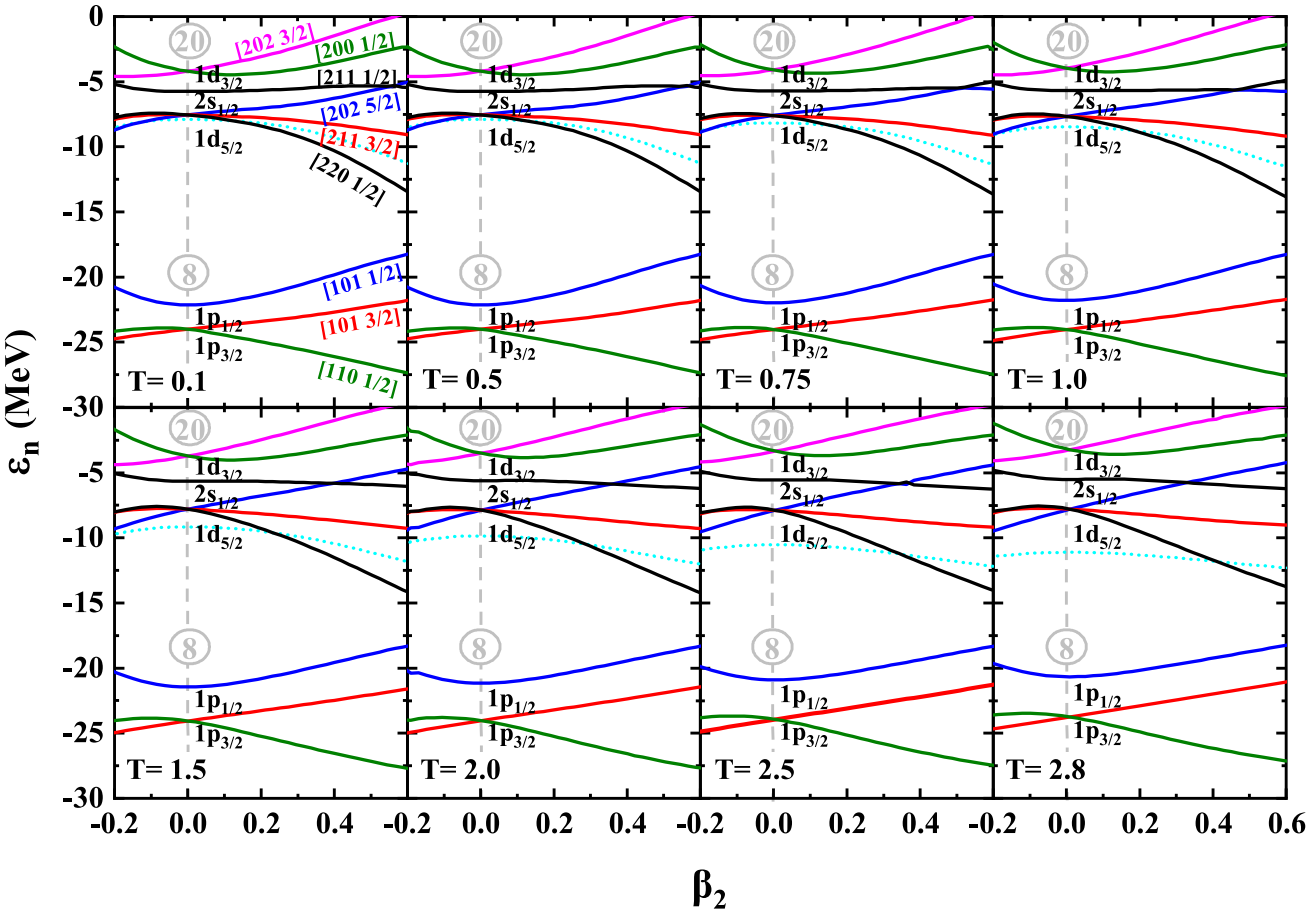

Fig. 5 (Color online) The neutron Nilsson single-particle level diagram (solid lines) as functions of quadrupole deformation β_2 at finite temperatures $T = 0.1$, 0.5, 0.75, 1.0, 1.5, 2.0, 2.5, and 2.8 MeV. The Fermi surface is indicated by the dotted curves

energy levels in comparison with neutron orbitals. As illustrated in Fig. 6, the temperature evolution of the hyperon single-particle energy levels closely resembles that of the neutron single-particle energy levels.

At low temperatures, the Λ hyperon exclusively occupies the $1s_{1/2}$ orbit, resulting in the Fermi surface coinciding with this orbit. As the temperature increases, the Fermi surface gradually shifts downward relative to the $1s_{1/2}$ orbit, and the splitting of the $1p_{3/2}$ orbit becomes enhanced, particularly at large quadrupole deformations. The occupancy probabilities of the hyperon orbitals undergo marked redistribution, indicating that thermal excitation increases the probability of hyperons occupying higher-energy states.

The observations of the downward shift of the Fermi energy and enhanced orbital splitting in both neutron and hyperon single-particle energy levels suggest a universal response of single-particle dynamics to thermal excitations in deformed nuclei.

The properties of the single-Λ hypernucleus ${}^{21}_{\Lambda}$Ne at different temperatures are listed in Table 1. The root-mean-square (rms) radii of protons and neutrons exhibit small variations with increasing temperature, remaining within the ranges of 2.87–2.89 fm and 2.90–2.92 fm, respectively. In contrast, the rms radius of the Λ hyperon increases from 2.52 fm to 2.62 fm over the same temperature range. This indicates that the nucleon distribution is relatively insensitive to temperature changes compared to the hyperon, because it is much easier to be influenced by the temperature for a single-Λ hyperon than for a large nucleus composed of many protons and neutrons whose center densities are less sensitive to temperature. This trend is consistent with the findings of Ref. [36].

At low temperatures ($T \leq 1.0$ MeV), nucleons are thermally excited from low-energy levels to high-energy orbitals near the Fermi surface, where they are more sensitive to the nuclear deformation potentials. This resulted in a slight increase in the overall deformation.

However, as the temperature exceeded 1.0 MeV, the deformation gradually decreased and eventually vanished at 2.8 MeV. This trend arises because higher temperatures lead to increased nucleon excitations from lower-energy states to higher-energy states, causing the nucleon distribution

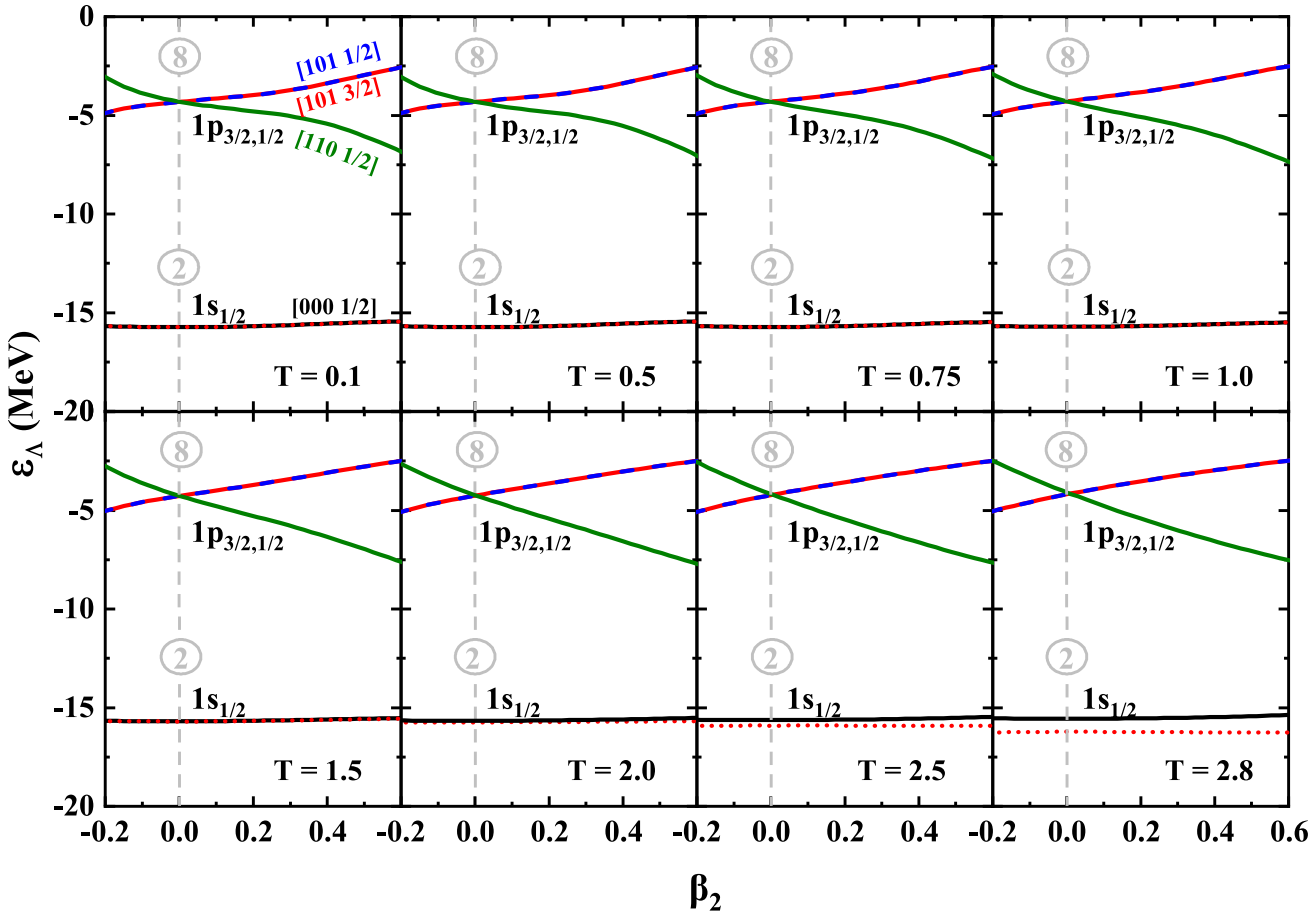

Fig. 6 (Color online) Same as Fig. 5, but for Λ hyperon

Table 1 For a given temperature T, calculated root-mean-squared radii $\langle r_q \rangle$ (q = n, p, and Λ), quadrupole deformation parameters β_{2q}, single-Λ binding energy B_Λ, entropy S, and occupation probabilities v^2 of the Λ hyperon in the 1s, 1p states in ${}^{21}_{\Lambda}$Ne

T	$\langle r_n \rangle$	$\langle r_p \rangle$	$\langle r_\Lambda \rangle$	β_{2n}	β_{2p}	$\beta_{2\Lambda}$	B_Λ	S	v^2		
(MeV)	(fm)	(fm)	(fm)				(MeV)		[000 1/2]	[110 1/2]	[101 1/2,3/2]
0.0	2.88	2.90	2.52	0.45	0.61	0.23	16.00	0.00	0.50	0.00	0.00
0.5	2.89	2.91	2.53	0.46	0.63	0.25	15.98	2.44	0.50	0.00	0.00
1.0	2.90	2.92	2.54	0.45	0.63	0.28	15.96	6.15	0.50	0.00	0.00
1.5	2.89	2.92	2.55	0.42	0.59	0.28	15.98	8.06	0.50	0.00	0.00
2.0	2.88	2.92	2.57	0.38	0.53	0.28	15.93	9.24	0.48	0.01	0.00
2.5	2.87	2.92	2.60	0.29	0.40	0.22	15.78	10.12	0.46	0.02	0.01
2.8	2.87	2.92	2.62	0.00	0.00	0.00	15.42	10.65	0.46	0.01	0.01

to become more uniform. Consequently, the Fermi surface smears, shell effects weaken, and deformation diminishes as the temperature increases.

Moreover, the single-Λ binding energy B_Λ is a key observable characterizing hypernuclear stability, which is defined as the difference between the hypernucleus and the core nucleus without a hyperon. B_Λ decreases monotonically with temperature, with the rate of decrease accelerating above $T > 2.0$ MeV. This behavior originates from the reduction of the hyperon potential with increasing temperature, leading to a decrease in the binding energy at higher temperatures. Simultaneously, the entropy S of the hypernuclear system increases with temperature, directly reflecting the enhanced thermal excitation of this system. As more particles transition from low-energy to high-energy states, the resulting broadening of the nucleon and hyperon wave functions leads to increased disorder in the quantum many-body system. In addition to the global quantities, the Λ hyperon occupation probabilities v^2 with temperature provide valuable microscopic insight into the thermal response of the hypernuclear

system. At low temperatures ($T \leq 1.5$ MeV), the Λ hyperon predominantly occupies the lowest s-orbit, [000 1/2], with an occupation probability close to $v^2 \approx 0.50$, whereas the p-shell states remain essentially unoccupied. As the temperature increases, thermal excitation leads to the partial population of higher-lying states. At $T = 2.0$ MeV, the occupation of the [110 1/2] state becomes noticeable, reaching $v^2 = 0.02$ by $T = 2.5$ MeV. Simultaneously, the [101 1/2] and [101 3/2] orbitals also began to acquire finite occupancy. It is important to note that, owing to the weak spin–orbit interaction for the Λ hyperon, the [101 1/2] and [101 3/2] orbitals are nearly degenerate and can be treated collectively.

To assess the robustness of the conclusion that cluster structures in ${}^{21}_{\Lambda}$Ne disappear with increasing temperature, we investigated the sensitivity of the results to variations in both YN and NN interactions. Several representative microscopic YN forces NSC97f, NSC97a, NSC89, and ESC08 were employed in combination with the Skyrme NN parameter set SkI4. The thermal evolution of the cluster structures exhibited negligible dependence on the choice of YN interaction, indicating that the presence of the Λ hyperon induces only subtle changes in the relative free energy surfaces.

In contrast, varying the NN interaction parameters (SkI3, SkI4, SLy4, and SLy5) produced more noticeable differences in the relative free energy surfaces, as shown in Fig. 7. The SkI3 and SkI4 results are similar, with clustering weakening as the temperature increased and vanishing at $T = 2.8$ MeV. In contrast, with SLy4 and SLy5, clustering disappeared at a lower temperature of $T = 2.2$ MeV. These differences are reflected in the slight shifts in the position and depth of the local minima on the free energy surface. However, the overall trend, clustering suppression with increasing temperature, remained unchanged, indicating that while the NN interaction affects the quantitative details, it does not alter the qualitative behavior.

These findings indicate that the temperature-induced delocalization in the deformed hypernucleus ${}^{21}_{\Lambda}$Ne represents a robust prediction within the FT-SHF framework, which is independent of the specific choice of the YN interaction. Although the selection of the NN interaction can affect the precise value of the critical temperature, it does not alter the general trend of temperature-driven delocalization in the system.

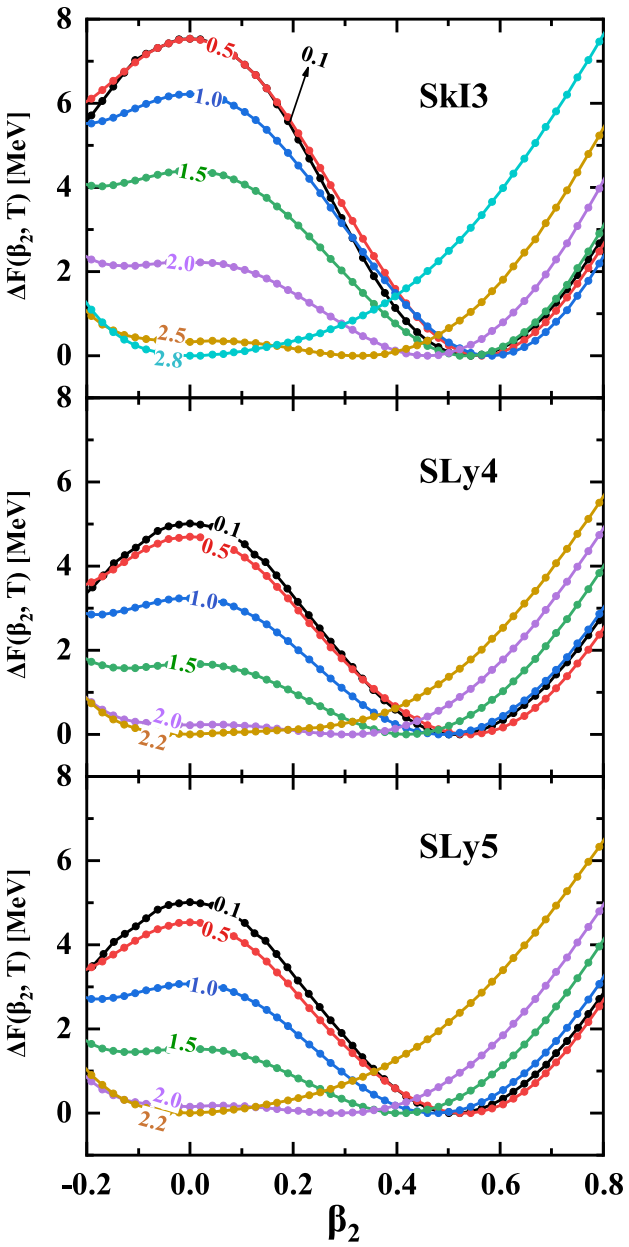

Fig. 7 (Color online) Relative free energies, $\Delta F(\beta_2, T)$, as functions of the quadrupole deformation parameter β_2, calculated at finite temperatures for ${}^{21}_{\Lambda}$Ne using three different Skyrme NN interactions: SkI3, SLy4, and SLy5. The YN interaction NSC97f in the calculations is the same

5 Summary

In this study, finite-temperature SHF calculations were performed to investigate the localization and clustering phenomena in hypernucleus ${}^{21}_{\Lambda}$Ne. For the nucleon–nucleon interaction, the Skyrme force SkI4 is adopted, while for the hyperon–nucleon interaction, the microscopic Nijmegen interaction NSC97f is employed.

By employing the total intrinsic density function in conjunction with the nucleon localization function, the clustering characteristics of the highly deformed ground state in ${}^{21}_{\Lambda}$Ne at zero temperature can be readily observed. The localization and clustering characteristics progressively diminished with escalating temperature, culminating in their complete disappearance upon reaching a threshold of 2.8 MeV. This is because temperature weakens deformation, suppressing the spatial localization of nucleons and hindering cluster

formation. Hence, the density spreads across the surface region and destroys localization characteristics.

Furthermore, we examined the effects of temperature on the neutron and hyperon Nilsson single-particle energy levels. As the temperature increases, the thermal excitations of nucleons enhance, leading to a downward shift of the Fermi surface and an enlarged orbital splitting. This effect is particularly pronounced in the well-deformed region, where the deformation-induced splitting of the energy levels becomes more significant with increasing temperature.

In addition, we investigated the temperature dependence of the radii, deformation, single-Λ binding energy, and entropy for ${}^{21}_{\Lambda}$Ne. The temperature-induced variation in the hyperon radius is more pronounced than that in the proton and neutron radii because the single hyperon is more easily excited than the numerous nucleons in the core.

Finally, it is demonstrated that the choice of NN interactions can affect the precise value of the critical temperature. However, the general trend of temperature-driven delocalization in the system is robust against NN and YN interactions.

Author Contributions All authors contributed to the study conception and design. Material preparation, data collection, and analysis were performed by Xin Li, Chao-Feng Chen, Qi-Bo Chen, and Xian-Rong Zhou. The first draft of the manuscript was written by Xin Li, and all authors commented on previous versions of the manuscript. All authors read and approved the final manuscript.

Data availability The data that support the findings of this study are openly available in Science Data Bank at https://cstr.cn/31253.11.sciencedb.j00186.00809 and https://doi.org/10.57760/sciencedb.j00186.00809.

Declarations

Conflict of interest The authors declare that they have no conflict of interest.

References

1. M. Danysz, J. Pniewski, Delayed disintegration of a heavy nuclear fragment: I. Philos. Mag. **44**, 348 (1953). https://doi.org/10.1080/14786440308520318
2. M. Isaka, M. Kimura, A. Dote et al., Deformation of hypernuclei studied with antisymmetrized molecular dynamics. Phys. Rev. C **83**, 044323 (2011). https://doi.org/10.1103/PhysRevC.83.044323
3. M. Isaka, H. Homma, M. Kimura et al., Modification of triaxial deformation and change of spectrum in ${}^{25}_{\Lambda}$Mg caused by the Λ hyperon. Phys. Rev. C **85**, 034303 (2012). https://doi.org/10.1103/PhysRevC.85.034303
4. J.W. Cui, X.R. Zhou, L.X. Guo et al., Investigation of single- and double-Λ hypernuclei using a beyond-mean-field approach. Phys. Rev. C **95**, 024323 (2017). https://doi.org/10.1103/PhysRevC.95.024323
5. E. Hiyama, M. Kamimura, K. Miyazaki et al., γ transitions in A=7 hypernuclei and a possible derivation of hypernuclear size. Phys. Rev. C **59**, 2351–2360 (1999). https://doi.org/10.1103/PhysRevC.59.2351
6. Y. Tanimura, Clusterization and deformation of multi-Λ hypernuclei within a relativistic mean-field model. Phys. Rev. C **99**, 034324 (2019). https://doi.org/10.1103/PhysRevC.99.034324
7. D. Vretenar, W. Pöschl, G.A. Lalazissis et al., Relativistic mean-field description of light Λ hypernuclei with large neutron excess. Phys. Rev. C **57**, R1060–R1063 (1998). https://doi.org/10.1103/PhysRevC.57.R1060
8. X.R. Zhou, A. Polls, H.J. Schulze et al., Λ hyperons and the neutron drip line. Phys. Rev. C **78**, 054306 (2008). https://doi.org/10.1103/PhysRevC.78.054306
9. Y. Zhang, J. Hu, P. Liu, Massive neutron star with strangeness in a relativistic mean-field model with a high-density cutoff. Phys. Rev. C **97**, 015805 (2018). https://doi.org/10.1103/PhysRevC.97.015805
10. G.F. Burgio, H.J. Schulze, I. Vidaña et al., Neutron stars and the nuclear equation of state. Prog. Part. Nucl. Phys. **120**, 103879 (2021). https://doi.org/10.1016/j.ppnp.2021.103879
11. Y.G. Ma, Hypernuclei as a laboratory to test hyperon-nucleon interactions. Nucl. Sci. Tech. **34**, 97 (2023). https://doi.org/10.1007/s41365-023-01248-6
12. J.H. Chen, F.K. Guo, Y.G. Ma et al., Production of exotic hadrons in pp and nuclear collisions. Nucl. Sci. Tech. **36**, 55 (2025). https://doi.org/10.1007/s41365-025-01664-w
13. W. Keil, H.T. Janka, Hadronic phase transitions at supranuclear densities and the delayed collapse of newly formed neutron stars. Astron. Astrophys. **296**, 145 (1995) https://adsabs.harvard.edu/full/1995A
14. Z. Yu, G.Z. Liu, M.F. Zhu et al., Thermal neutron stars including the hyperon-hyperon interactions. Nucl. Phys. A **834**, 97c–99c (2010). https://doi.org/10.1016/j.nuclphysa.2010.01.029
15. M. Oertel, F. Gulminelli, C. Providência et al., Hyperons in neutron stars and supernova cores. Eur. Phys. J. A **52**, 1–22 (2016). https://doi.org/10.1140/epja/i2016-16050-1
16. A.S. Botvina, K.K. Gudima, J. Steinheimer et al., Formation of hypernuclei in heavy-ion collisions around the threshold energies. Phys. Rev. C **95**, 014902 (2017). https://doi.org/10.1103/PhysRevC.95.014902
17. P. Liu, J.H. Chen, Y.G. Ma et al., Production of light nuclei and hypernuclei at high intensity accelerator facility energy region. Nucl. Sci. Tech. **28**, 55 (2017). https://doi.org/10.1007/s41365-017-0207-x
18. Z.Q. Feng, Formation and dynamics of exotic hypernuclei in heavy-ion collisions. Phys. Rev. C **102**, 044604 (2020). https://doi.org/10.1103/PhysRevC.102.044604
19. J. Adam, L. Adamczyk, J.R. Adams et al., Global polarization of Λ hyperons in Au + Au collisions at $\sqrt{s_{NN}} = 200$ Gev. Phys. Rev. C **98**, 014910 (2018). https://doi.org/10.1103/PhysRevC.98.014910
20. J. Adam et al., Measurement of the mass difference and the binding energy of the hypertriton and antihypertriton. Nat. Phys. **16**, 409–412 (2020). https://doi.org/10.1038/s41567-020-0799-7
21. B. Dönigus et al., (Anti-)matter and hyper-matter production at the LHC with ALICE. Nucl. Phys. A **904**, 547c–550c (2013). https://doi.org/10.1016/j.nuclphysa.2013.02.073
22. B. Dönigus et al., Exotica production with alice. Eur. Phys. J. Web Conf. **97**, 00013 (2015). https://doi.org/10.1051/epjconf/20159700013
23. T.R. Saito, D. Nakajima, C. Rappold et al., Production of hypernuclei in peripheral HI collisions: the HypHI project at GSI. Nucl. Phys. A **881**, 218–227 (2012). https://doi.org/10.1016/j.nuclphysa.2012.02.011

24. K.T. Brinkmann, P. Gianotti, I. Lehmann, Exploring the mysteries of strong interactions—the panda experiment. Nucl. Phys. News **16**, 15–18 (2006). https://doi.org/10.1080/10506890600579868
25. I. Vassiliev, P. Senger, I. Kisel et al., Hypernuclei program at the CBM experiment. JPS Conf. Proc. **17**, 092001 (2017). https://doi.org/10.7566/JPSCP.17.092001
26. C. Rappold, J. López-Fidalgo, Examination of experimental conditions for the production of proton-rich and neutron-rich hypernuclei. Phys. Rev. C **94**, 044616 (2016). https://doi.org/10.1103/PhysRevC.94.044616
27. Y.B. Ivanov, A.A. Soldatov, Vorticity in heavy-ion collisions at the JINR nuclotron-based ion collider facility. Phys. Rev. C **95**, 054915 (2017). https://doi.org/10.1103/PhysRevC.95.054915
28. X. Chen, J. Yang, J. Xia et al., Study of eddy current effect in BRing at HIAF. Nucl. Instrum. Methods A **920**, 37–42 (2019). https://doi.org/10.1016/j.nima.2018.10.206
29. J.L. Rodríguez-Sánchez, J. Cugnon, J.C. David et al., Hypernuclei formation in spallation reactions by coupling the liège intranuclear cascade model to the deexcitation code abla. Phys. Rev. C **105**, 014623 (2022). https://doi.org/10.1103/PhysRevC.105.014623
30. V. Topor Pop, S. Das Gupta, Model for hypernucleus production in heavy ion collisions. Phys. Rev. C **81**, 054911 (2010). https://doi.org/10.1103/PhysRevC.81.054911
31. P. Braun-Munzinger, B. Dönigus, Loosely-bound objects produced in nuclear collisions at the LHC. Nucl. Phys. A **987**, 144–201 (2019). https://doi.org/10.1016/j.nuclphysa.2019.02.006
32. S. Reddy, M. Prakash, J.M. Lattimer et al., Effects of strong and electromagnetic correlations on neutrino interactions in dense matter. Phys. Rev. C **59**, 2888–2918 (1999). https://doi.org/10.1103/PhysRevC.59.2888
33. L.F. Roberts, G. Shen, V. Cirigliano et al., Protoneutron star cooling with convection: The effect of the symmetry energy. Phys. Rev. Lett. **108**, 061103 (2012). https://doi.org/10.1103/PhysRevLett.108.061103
34. A.S. Botvina, N. Buyukcizmeci, A. Ergun et al., Formation of hypernuclei in evaporation and fission processes. Phys. Rev. C **94**, 054615 (2016). https://doi.org/10.1103/PhysRevC.94.054615
35. A. Ravlić, E. Yüksel, T. Nikšić et al., Expanding the limits of nuclear stability at finite temperature. Nat. Commun. **14**, 4834 (2023). https://doi.org/10.1038/s41467-023-40613-2
36. J. Hu, Z. Zhang, S. Bao et al., Phase transition in hot Λ hypernuclei within the relativistic thomas-fermi approximation. Phys. Rev. C **94**, 054325 (2016). https://doi.org/10.1103/PhysRevC.94.054325
37. B. Suleymanli, K. Bozkurt, E. Khan et al., Effects of finite temperature and pairing correlations in multi-Λ hypernuclei. Phys. Rev. C **110**, 014329 (2024). https://doi.org/10.1103/PhysRevC.110.014329
38. S.S. Avancini, M. Ferreira, H. Pais et al., Light clusters and pasta phases in warm and dense nuclear matter. Phys. Rev. C **95**, 045804 (2017). https://doi.org/10.1103/PhysRevC.95.045804
39. T. Custódio, A. Falcão, H. Pais et al., Light clusters in warm stellar matter: calibrating the cluster couplings. Eur. Phys. J. A **56**, 295 (2020). https://doi.org/10.1140/epja/s10050-020-00302-w
40. G. Röpke, Light nuclei quasiparticle energy shifts in hot and dense nuclear matter. Phys. Rev. C **79**, 014002 (2009). https://doi.org/10.1103/PhysRevC.79.014002
41. K. Sumiyoshi, G. Röpke, Appearance of light clusters in post-bounce evolution of core-collapse supernovae. Phys. Rev. C **77**, 055804 (2008). https://doi.org/10.1103/PhysRevC.77.055804
42. Z. Ren, S. Elhatisari, T.A. Lähde et al., Ab initio study of nuclear clustering in hot dilute nuclear matter. Phys. Lett. B **850**, 138463 (2024). https://doi.org/10.1016/j.physletb.2024.138463
43. E. Yüksel, F. Mercier, J.P. Ebran et al., Clustering in nuclei at finite temperature. Phys. Rev. C **106**, 054309 (2022). https://doi.org/10.1103/PhysRevC.106.054309
44. B. Li, D. Vretenar, Z.X. Ren et al., Fission dynamics, dissipation, and clustering at finite temperature. Phys. Rev. C **107**, 014303 (2023). https://doi.org/10.1103/PhysRevC.107.014303
45. A.L. Goodman, Finite-temperature HFB theory. Nucl. Phys. A **352**, 30–44 (1981). https://doi.org/10.1016/0375-9474(81)90557-1
46. Y.F. Niu, Z.M. Niu, N. Paar et al., Pairing transitions in finite-temperature relativistic hartree-bogoliubov theory. Phys. Rev. C **88**, 034308 (2013). https://doi.org/10.1103/PhysRevC.88.034308
47. J.J. Li, J. Margueron, W.H. Long et al., Pairing phase transition: A finite-temperature relativistic hartree-fock-bogoliubov study. Phys. Rev. C **92**, 014302 (2015). https://doi.org/10.1103/PhysRevC.92.014302
48. A. Ravlić, Y.F. Niu, T. Nikšić et al., Finite-temperature linear response theory based on relativistic hartree bogoliubov model with point-coupling interaction. Phys. Rev. C **104**, 064302 (2021). https://doi.org/10.1103/PhysRevC.104.064302
49. M. Bender, P.H. Heenen, P.G. Reinhard, Self-consistent mean-field models for nuclear structure. Rev. Mod. Phys. **75**, 121–180 (2003). https://doi.org/10.1103/RevModPhys.75.121
50. J.R. Stone, P.G. Reinhard, The Skyrme interaction in finite nuclei and nuclear matter. Prog. Part. Nucl. Phys. **58**, 587–657 (2007). https://doi.org/10.1016/j.ppnp.2006.07.001
51. E.B. Huo, K.R. Li, X.Y. Qu et al., Continuum Skyrme Hartree–Fock–Bogoliubov theory with Green's function method for neutron-rich Ca, Ni, Zr, and Sn isotopes. Nucl. Sci. Tech. **34**, 105 (2023). https://doi.org/10.1007/s41365-023-01261-9
52. X.R. Zhou, H.J. Schulze, H. Sagawa et al., Hypernuclei in the deformed Skyrme–Hartree–Fock approach. Phys. Rev. C **76**, 034312 (2007). https://doi.org/10.1103/PhysRevC.76.034312
53. H.J. Schulze, T. Rijken, Hypernuclear structure with the Nijmegen ESC08 potentials. Phys. Rev. C **88**, 024322 (2013). https://doi.org/10.1103/PhysRevC.88.024322
54. H.J. Schulze, E. Hiyama, Skyrme force for light and heavy hypernuclei. Phys. Rev. C **90**, 047301 (2014). https://doi.org/10.1103/PhysRevC.90.047301
55. J. Guo, X.R. Zhou, H.J. Schulze, Skyrme force for all known Ξ^- hypernuclei. Phys. Rev. C **104**, L061307 (2021). https://doi.org/10.1103/PhysRevC.104.L061307
56. C.F. Chen, Q.B. Chen, X.R. Zhou et al., Effects of hyperons on the deformations of even–even nuclei *. Chin. Phys. C **46**, 064109 (2022). https://doi.org/10.1088/1674-1137/ac5b58
57. J. Guo, C.F. Chen, X.R. Zhou et al., ΛΛ pairing effects in spherical and deformed multi-Λ hyperisotopes. Phys. Rev. C **105**, 034322 (2022). https://doi.org/10.1103/PhysRevC.105.034322
58. H.T. Xue, Y.F. Chen, Q.B. Chen et al., Deformation and spin–orbit splitting of Λ hypernuclei in the Skyrme–Hartree–Fock approach. Phys. Rev. C **107**, 044317 (2023). https://doi.org/10.1103/PhysRevC.107.044317
59. H.T. Xue, J.W. Cui, Q.B. Chen et al., Shape coexistence in ne isotopes and hyperon impurity effect on low-lying states. Phys. Rev. C **110**, 044310 (2024). https://doi.org/10.1103/PhysRevC.110.044310
60. P.G. Reinhard, J.A. Maruhn, A.S. Umar et al., Localization in light nuclei. Phys. Rev. C **83**, 034312 (2011). https://doi.org/10.1103/PhysRevC.83.034312
61. T. Ichikawa, J.A. Maruhn, N. Itagaki et al., Linear chain structure of four-α clusters in ^{16}O. Phys. Rev. Lett. **107**, 112501 (2011). https://doi.org/10.1103/PhysRevLett.107.112501
62. Y. Fukuoka, S. Shinohara, Y. Funaki et al., Deformation and cluster structures in^{12}C studied with configuration mixing using skyrme interactions. Phys. Rev. C **88**, 014321 (2013). https://doi.org/10.1103/PhysRevC.88.014321

63. X. Li, C.F. Chen, X.R. Zhou et al., Clusterization and localization of multi-Λ hyperisotopes. Phys. Rev. C **109**, 064301 (2024). https://doi.org/10.1103/PhysRevC.109.064301
64. B. Zhou, Y. Funaki, H. Horiuchi et al., Nonlocalized clustering: A new concept in nuclear cluster structure physics. Phys. Rev. Lett. **110**, 262501 (2013). https://doi.org/10.1103/PhysRevLett.110.262501
65. Y. Kanada-En'yo, K. Ogata, Properties of $K^\pi = 0_1^+$, $K^\pi = 2^-$, and $K^\pi = 0_1^-$ bands of ^{20}Ne probed via proton and α inelastic scattering. Phys. Rev. C **101**, 064308 (2020). https://doi.org/10.1103/PhysRevC.101.064308
66. B. Zhou, Y. Funaki, H. Horiuchi et al., The 5α condensate state in ^{20}Ne. Nat. Commun. **14**, 8206 (2023). https://doi.org/10.1038/s41467-023-43816-9
67. T. Kawabata, The 5α condensate state in ^{20}Ne. Nucl. Sci. Tech. **35**, 35 (2024). https://doi.org/10.1007/s41365-024-01385-6
68. M. Rayet, Self-consistent calculations of hypernuclear properties with the Skyrme interaction. Ann. Phys. **102**, 226–251 (1976). https://doi.org/10.1016/0003-4916(76)90262-1
69. H.J. Schulze, Skyrme forces for lambda and cascade hypernuclei. AIP Conf. Proc. **2130**, 020009 (2019). https://doi.org/10.1063/1.5118377
70. T.T. Sun, E. Hiyama, H. Sagawa et al., Mean-field approaches for Ξ^- hypernuclei and current experimental data. Phys. Rev. C **94**, 064319 (2016). https://doi.org/10.1103/PhysRevC.94.064319
71. P. Bonche, S. Levit, D. Vautherin, Properties of highly excited nuclei. Nucl. Phys. A **427**, 278–296 (1984). https://doi.org/10.1016/0375-9474(84)90086-1
72. P.G. Reinhard, B. Schuetrumpf, J. Maruhn, The axial Hartree–Fock + BCS code SkyAx. Comput. Phys. Commun. **258**, 107603 (2021). https://doi.org/10.1016/j.cpc.2020.107603
73. D. Vautherin, D.M. Brink, Hartree–Fock calculations with Skyrme's interaction. I. Spherical nuclei. Phys. Rev. C **5**, 626–647 (1972). https://doi.org/10.1103/PhysRevC.5.626
74. D. Vautherin, Hartree–Fock calculations with Skyrme's interaction. II. Axially deformed nuclei. Phys. Rev. C **7**, 296–316 (1973). https://doi.org/10.1103/PhysRevC.7.296
75. M. Rayet, Skyrme parametrization of an effective Λ-nucleon interaction. Nucl. Phys. A **367**, 381–397 (1981). https://doi.org/10.1016/0375-9474(81)90655-2
76. P.G. Reinhard, H. Flocard, Nuclear effective forces and isotope shifts. Nucl. Phys. A **584**, 467–488 (1995). https://doi.org/10.1016/0375-9474(94)00770-N
77. E. Chabanat, P. Bonche, P. Haensel et al., A Skyrme parametrization from subnuclear to neutron star densities Part II. Nuclei far from stabilities. Nucl. Phys. A **635**, 231–256 (1998). https://doi.org/10.1016/S0375-9474(98)00180-8
78. V. Martin, J.L. Egido, L.M. Robledo, Thermal shape fluctuation effects in the description of hot nuclei. Phys. Rev. C **68**, 034327 (2003). https://doi.org/10.1103/PhysRevC.68.034327
79. J.L. Egido, P. Ring, The decay of hot nuclei. J. Phys. G: Nucl. Part. Phys. **19**, 1 (1993). https://doi.org/10.1088/0954-3899/19/1/002
80. J.L. Egido, Quantum versus statistical fluctuations in mean-field theories. Phys. Rev. Lett. **61**, 767–770 (1988). https://doi.org/10.1103/PhysRevLett.61.767
81. A.L. Goodman, Statistical fluctuations in the $i_{\frac{13}{2}}$ model. Phys. Rev. C **29**, 1887–1896 (1984). https://doi.org/10.1103/PhysRevC.29.1887
82. E. Khan, N. Van Giai, N. Sandulescu. Nucl. Phys. A **789**, 94–102 (2007). https://doi.org/10.1016/j.nuclphysa.2007.03.005
83. J.A. Sheikh, W. Nazarewicz, J.C. Pei, Systematic study of fission barriers of excited superheavy nuclei. Phys. Rev. C **80**, 011302 (2009). https://doi.org/10.1103/PhysRevC.80.011302
84. R. Lisboa, M. Malheiro, B.V. Carlson, Dirac–Hartree–Bogoliubov calculation for spherical and deformed hot nuclei: temperature dependence of the pairing energy and gaps, nuclear deformation, nuclear radii, excitation energy, and entropy. Phys. Rev. C **93**, 024321 (2016). https://doi.org/10.1103/PhysRevC.93.024321
85. J.P. Ebran, E. Khan, T. Nikšić et al., Localization and clustering in the nuclear Fermi liquid. Phys. Rev. C **87**, 044307 (2013). https://doi.org/10.1103/PhysRevC.87.044307
86. E. Khan, L. Heitz, F. Mercier et al., α-particle formation and clustering in nuclei. Phys. Rev. C **106**, 064330 (2022). https://doi.org/10.1103/PhysRevC.106.064330
87. E.F. Zhou, J.M. Yao, Z.P. Li et al., Anatomy of molecular structures in ^{20}Ne. Phys. Lett. B **753**, 227–231 (2016). https://doi.org/10.1016/j.physletb.2015.12.028